Title

Quantifying Hydroxyl Adsorption on Copper with Electrochemical-Aware Random Phase Approximation

Journal

Journal of Chemical Theory and Computation, 22(11)

ISSN

1549-9618

Authors

Cheng, Dongfang
Chen, Dongxiao
Liu, Qian-Yu
et al.

Publication Date

2026-05-21

DOI

10.1021/acs.jctc.6c00353

Quantifying Hydroxyl Adsorption on Copper with Electrochemical-Aware Random Phase Approximation

Dongfang Cheng[1], Dongxiao Chen[1], Qianyu Liu[1], Ziyang Wei[2,3], Philippe Sautet[1,2,4]*

[1]Department of Chemical and Biomolecular Engineering, University of California, Los Angeles, CA 90095, USA.
[2]Department of Chemistry and Biochemistry, University of California, Los Angeles, CA 90095, USA.
[3]Department of Mechanical and Aerospace Engineering, Princeton University, Princeton, NJ 08544, USA.
[4]California NanoSystems Institute, Los Angeles, CA 90095, USA.

* Correspondence: sautet@ucla.edu

Abstract Accurate adsorption thermodynamics of reactive intermediates at electrified metal interfaces are central to predictive surface science, heterogeneous catalysis, and electrochemical modeling, yet remain challenging for standard density functional approximations and difficult to benchmark experimentally. Here we apply electrochemical-aware random phase approximation (RPA) methods that incorporate solvent dielectric screening and grand-canonical constant-potential control to establish a reference-quality description of hydroxyl (*OH) adsorption on Cu(100) in electrocatalytic conditions. At the potential of zero charge (*pzc*), we quantify the site dependence of *OH binding across terrace sites and representative defective motifs. Under applied potential, electrochemical-aware RPA reproduces the experimentally inferred *OH desorption fingerprint, predicting an *OH desorption potential of -0.54 V vs SHE, in excellent agreement with experimental value -0.56 V vs SHE at pH = 7, whereas widely used GGA functionals (PBE, RPBE) underestimate *OH stability and compress the stability window under reducing conditions. G_0W_0-RPA electronic structure analysis provides a mechanistic rationale for the discrepancy. Finally, we reassess the Cu(100) surface-state diagram with *OH and *CO co-adsorption under electrochemical conditions, including the stability of metastable $CuCO(OH)_n$ motifs, and show that many-body accuracy can qualitatively alter predicted interfacial speciation. Overall, our results establish electrochemical-aware RPA as a broadly applicable, systematically improvable many-body framework for quantitative adsorption thermodynamics at constant potential, enabling predictive surface-state maps for complex electrochemical interfaces.

1. Introduction

Accurately describing adsorption at metal or metal oxide surfaces is a prerequisite for predictive surface science and heterogeneous catalysis, because adsorption free energies govern coverages, reaction thermochemistry, and ultimately selectivity[1]. Most atomistic mechanistic studies therefore rely on Kohn-Sham density functional theory (DFT), commonly with generalized-gradient-approximation (GGA) functionals[2,3], due to their favorable cost and broad applicability. For

molecular adsorbates on well-defined single-crystal surfaces, experimental tools like temperature-programmed desorption (TPD)[4–7], Fourier transform infrared (FTIR) spectroscopy[8,9] have long been used to infer desorption barriers/energetics, and related calorimetric approaches as single crystal adsorption calorimetry (SCAC) can directly access adsorption enthalpies under controlled conditions[5,10]. However, benchmarking becomes substantially more difficult for reactive intermediates and radical-like surface species that are short-lived, present at low steady-state coverage, or undergo rapid interconversion, and limitations that are amplified under electrochemical conditions, where solvent dielectric screening and electrode potential complicate both surface speciation and measurement.

On the theory side, semi-local DFT GGA functionals are known to miss chemical accuracy for key chemisorption problems[11–14], famously exemplified by the 'CO puzzle problem', highlighting that GGA errors can be qualitative rather than merely quantitative[15–18]. Including van der Waals corrections, or moving to meta-GGA or hybrid functionals, can improve adsorption energetics in some cases, but often degrade the accuracy of surface energies because of an intrinsic tradeoff rooted in the underlying linear scaling relationships[15]. Methods beyond DFT, including coupled-cluster theory[19–21] and quantum Monte Carlo[22–24], provide systematic routes to higher accuracy, but only a subset are practical for periodic surfaces at catalysis-relevant complexity due to the exponential scaling with the system size[25]. A further challenge is that many high-level electronic-structure methods were developed primarily for neutral, vacuum interfaces, whereas electrochemical environments require both solvent dielectric screening and control of electrode potential. Electron grand canonical (GC) approaches[26–28] are especially important because adsorption and surface charging are coupled, and fixed-charge approximations can misrepresent potential-dependent stability windows, yet GC formalisms have most often been implemented within DFT[29], despite being highly desirable for advanced electronic-structure methods.

The random phase approximation (RPA)[30,31], a post-Hartree-Fock (HF) method within many-body perturbation theory[32,33], is particularly attractive as a reference framework for surfaces because it is non-empirical, captures long-range correlation and dispersion at the many-body level, and has shown robust accuracy for adsorption energetics and surface stability across transition-metal surfaces while remaining feasible in periodic settings[15,34]. Recently, we developed electrochemistry-oriented extensions of RPA that incorporate (i) solvation effects via an RPA–linearized Poisson-Boltzmann (LPB) framework (RPA-sol)[35] and (ii) a full GC treatment of RPA (GC-RPA) to capture the electrode potential effects[36]. Using these methods, we have quantified potential-dependent adsorption thermodynamics and resolved key mechanistic questions in electrochemical CO_2 reduction reaction (CO_2RR), including potential-determining steps[35], proton sources[37], and the potential dependence of CO adsorption on Cu[36].

Nevertheless, quantitative benchmarks for radical-like adsorbates, especially under electrochemical conditions, remain rare. A representative and mechanistically important case is hydroxyl (*OH) adsorption on Cu surfaces, which leaves a clear electrochemical fingerprint in cyclic voltammetry. Early single-crystal studies in alkaline electrolyte reported a distinct OH-

related adsorption/desorption region on Cu(100) spanning -1.13 to -0.83 V vs SHE[38], underscoring that oxygenated surface species can be stabilized at a potential well below that of oxide formation. Koper and co-workers[39] further showed that the Cu(100) CV measured in alkaline electrolyte is very similar to the CV previously reported by Waegele et al. in near-neutral electrolyte[40], and on this basis assigned the corresponding pair of peaks (-0.56 V vs SHE) to OH adsorption/desorption[39]. Recent *in-situ* Raman spectroscopy results pointed out that *OH can exist on Cu surfaces even at very negative potentials (-1 V vs RHE) during CO_2RR in alkaline conditions[41,42]. Strikingly, despite this experimentally implied stability window, DFT-GGA descriptions often predict *OH to be stable over a much narrower potential range (or destabilized too early under reducing conditions)[37,41], potentially biasing predicted surface states and mechanistic interpretations when *OH co-adsorbs with key intermediates (e.g., CO) during CO_2RR.

In this work, we use electrochemical-aware RPA to establish a reference-quality description of *OH adsorption on Cu(100) under electrochemical conditions. We first access the site dependence of *OH adsorption on Cu(100) terrace sites and extend the analysis to representative defects, Cu adatoms and vacancies, at the potential of zero charge (*pzc*) using RPA-sol. We then benchmark the transferability and internal consistency of two constant-potential routes, fully grand-canonical treatment of RPA (GC-RPA) and an RPA-GCDFT extrapolation strategy, for predicting the *OH desorption potential on Cu(100) in electrochemical conditions. This validation enables the reproduction of the experimental thermodynamic fingerprint: RPA yields an *OH desorption potential of -0.54 V vs SHE, in excellent agreement with the experimentally inferred value of -0.56 V vs SHE at pH = 7, whereas common DFT-GGA functionals (e.g., PBE and RPBE) prematurely destabilize *OH and predict an artificially narrow stability window under reducing conditions. We then use *GW*-RPA electronic structure analysis to identify the physical origin of this discrepancy. Finally, motivated by the long-standing CO adsorption puzzle, we revisited the Cu(100) Pourbaix diagram under *OH and *CO co-adsorption, including the stability of metastable $CuCO(OH)_n$ motifs. Overall, our results demonstrate that electrochemical-aware RPA provides a robust and general framework for radical adsorption thermodynamics under electrochemical conditions, enabling quantitatively reliable surface-state predictions that are critical for mechanistic studies of electrochemical interfaces.

2. Methods

2.1. Random phase approximation (RPA) with implicit solvent. We calculated total energies using the Adiabatic Connection Fluctuation Dissipation Theorem (ACFDT)[32] in its RPA, a method originating from many body perturbation theory that has been reformulated within the framework of density functional theory. The total energy expression within RPA can be written as[43]:

$$E^{RPA} = E^{EXX}\left(\left[\Psi_{occ,vaccum}\right]\right) + E_c^{RPA}\left(\left[\Psi_{occ,vaccum}, \Psi_{uocc,vaccum}\right]\right) \quad (1)$$

where E^{RPA} denotes the RPA total energy. This energy is composed of E^{EXX} the exact exchange energy, which only depends on the occupied orbitals $\Psi_{occ,vaccum}$, and the RPA correlation energy E_c^{RPA}, which depends on all occupied and unoccupied $\Psi_{occ,vaccum}$ and $\Psi_{uocc,vaccum}$.[44,45]

First, the orbitals considering solvation effects at the DFT level can be obtained using the linearized Poisson-Boltzmann (LPB) equation, as implemented by Hennig et al.[29]. Consequently, the occupied orbitals with the presence of implicit solvation, $\Psi_{occ,solvation}$, are derived. The unoccupied orbitals, $\Psi_{uocc,solvation}$, are obtained through a diagonalization step, as done in typical RPA calculations. Using these orbitals and incorporating the solvation energy, based on the electron density determined by the occupied orbitals, allows us to compute RPA energetics that include implicit solvation effects.

$$E_{sol}^{RPA} = E^{EXX}\left(\left[\Psi_{occ,solvation}\right]\right) + E_c^{RPA}\left(\left[\Psi_{occ,solvation}, \Psi_{uocc,solvation}\right]\right) + E^{solvation}\left(\left[\Psi_{occ,solvation}\right]\right) \quad (2)$$

where the solvation energy $E^{solvation}\left(\left[\Psi_{occ,solvation}\right]\right)$ is obtained in the non-self-consistent HF step, and essentially this term only depends on the charge density. Nevertheless, the RPA-sol energy is not simply the vacuum RPA energy plus this solvation energy: the orbitals including the influence of implicit solvation, $\Psi_{occ/uocc,solvation}$, give nontrivial contribution to the exchange and correlation components in the RPA-sol energy as well. In this work, all RPA energies are considered as RPA-sol energies unless otherwise specified.

2.2. Grand canonical treatment of RPA. We first briefly revisit the grand canonical treatment of DFT (GCDFT). In the computational hydrogen electrode (CHE) approach[46], the total chemical potential of the proton-electron pair as a function of applied potential, at all temperature T and pH values, can be calculated as:

$$\mu(H^+) + \mu(e^-) = \frac{1}{2}G(H_2) - ln(10)k_BT \cdot pH - eU_{SHE} \quad (3)$$

Where $G(H_2)$ is the free energy of the gas phase H_2 molecule at $P = 1$ bar and U_{SHE} is the potential referenced to the standard hydrogen electrode. The surface charging (SC) method is within the framework of GCDFT. Details can be found in our previous work[26,47], and here we summarize the key points.

The DFT energy for charged states ($E_{surface}$) is obtained as:

$$E_{surface} = E_{surface,raw} + n_{surface}\,\varepsilon_{Fermi\ shift} \quad (4)$$

Where $E_{surface,raw}$ is the raw energy output by VASP and $n_{surface}$ is the net number of the electrons of the surface. $n_{surface}\,\varepsilon_{Fermi\ shift}$ is the necessary correction term accounting for the difference ($\varepsilon_{Fermi\ shift}$) in the reference energy of the electron between the "internal" reference level and vacuum level.

Thus, the grand canonical electronic energy of a surface model, $\Omega(U)$, is obtained as:

$$\Omega(U) = E_{surface} - n_{surface}\,\mu_{electron} \quad (5)$$

Where $\mu_{electron}$ is the chemical potential of electron, which is defined as:

$$\mu_{electron} = qU_{vac} = -eU_{vac} \quad (6)$$

where U_{vac} is the potential of the system with reference to the vacuum level and q is the charge of an electron. In the implementation of Hennig and co-workers[48], the electrode potential referenced to vacuum is obtained by combining the Fermi level ε_F reported relative to an internal zero of energy with the Fermi shift, defined as the offset between this internal reference and the vacuum level:

$$-eU_{vac} = \varepsilon_F + \varepsilon_{Fermi\,shift} \quad (7)$$

For the metallic systems, the potential-dependent grand canonical energy, $\Omega(U)$, exhibits a quadratic behavior around the potential of zero charge (U_0) in the vacuum scale:

$$\Omega(U) = \Omega(U_0) - \frac{1}{2}C(U - U_0)^2 \quad (8)$$

Where C is the capacitance of the surface. The potential of the system with respect to the standard hydrogen electrode (SHE) can be converted from U_{vac} as:

$$U_{SHE}(GCDFT) = U_{vac} - 4.44 \quad (9)$$

We refer to this scheme as 'SCF approach' since the fermi level (ε_F) is obtained directly from self-consistent DFT calculations. In contrast, within the present periodic RPA implementation the total energy is evaluated in a single-shot manner on top of underlying DFT orbitals and one-electron energies. A self-consistent many-body electronic structure is therefore not available, and neither is a self-consistent ε_F. As a result, the SCF approach, which requires ε_F, cannot be applied directly at the non-self-consistent RPA level. To circumvent this limitation, we have introduced an alternative energetic approach that does not rely on a self-consistent electronic structure[36]. The key idea is to extract the electronic chemical potential from total-energy differences, using the thermodynamic relation between the internal energy E and chemical potential μ. Specifically:

$$\varepsilon_F = \mu_{electron} - \varepsilon_{Fermi\,shift} = \frac{\partial E_{surface}}{\partial n_{electron}} - \varepsilon_{Fermi\,shift} = \frac{\partial E_{surface,raw}}{\partial n_{electron}} \quad (10)$$

After computing RPA total energies for a series of charged slabs and fitting the resulting $E(n_{surface})$ data to a quadratic form, the electronic chemical potential (and thus the ε_F) can be obtained analytically from the derivative of the fit. Because the derivative of a quadratic function is linear, the resulting ε_F is expressed as a linear function of the electron number. Note that our previous work found that fitted ΔU_{SHE} obtained within GC-RPA was 5.31 V, which is larger than the widely accepted IUPAC value of 4.44 V. We adopted 5.31 V this work for consistency and discussed the effect of the absolute SHE references in Supplementary note 1.

$$U_{SHE}\,(GCRPA) = U_{vac} - 5.31 \quad (11)$$

2.3. RPA-SC extrapolation energetics. The GC-RPA requires extra computational cost and is not affordable for many practical systems. Therefore, we presented the extrapolated RPA-SC energetics using RPA-N, PBE-SC, and PBE-N energetics (N represents the neutral condition)[35,37]. Note that all PBE extrapolations are based on the most stable geometries obtained from self-consistent PBE calculations, using binding sites as identified by RPA.

$$\Delta\Omega^{RPA-SC}_{extroplated}(U) = \Delta\Omega^{RPA-N} + \Delta\Omega^{PBE-SC}(U) - \Delta\Omega^{PBE-N} \quad (12)$$

Where $\Delta\Omega^{RPA-N}$ and $\Delta\Omega^{PBE-N}$ are the adsorption free energy in neutral conditions at RPA and PBE level, respectively. $\Delta\Omega^{PBE-SC}(U)$ and $\Delta\Omega^{RPA-SC}_{extroplated}(U)$ are the potential-dependent adsorption free energy calculated grand canonically at PBE level and RPA level via extrapolation, respectively.

For all SC calculations, symmetric slabs consisting of five layers were used, created by symmetrizing the three-layer, 3×2 cell slab models. A slab separation of at least 60 Å (> 15 λ_D where λ_D is the Debye screening length) was used to ensure the convergence of the electrolyte density. The symmetric setup ensures that the vacuum level converges effectively by avoiding potential artifacts in the vacuum region caused by asymmetric charge distributions.

2.4. RPA Energetics Details. All RPA energetics in this work were based on PBE geometries. This choice is justified as the overbinding tendency of the PBE functional compensates for non-description of the weak van der Waals (vdW) interactions. Furthermore, the PBE-calculated lattice parameter for Cu (3.629 Å) and surface energy for Cu(100) (1.488 J/m²) are closer to the RPA values (3.581 Å and 1.914 J/m²) than those obtained using the RPBE functional (3.672 Å and 1.257 J/m²)[34]. The focus on both occupied and unoccupied orbitals in RPA calculations introduces two main challenges: First, the true orbitals are unknown and are typically approximated by those obtained from semi-local DFT functionals. In this study, we rely on RPA calculations using the PBE-derived orbitals and one-electron energies (RPA@PBE) since our previous benchmarks showed that using orbitals from PBE and RPBE yield nearly identical results[34]. Second, although an infinite number of unoccupied orbitals theoretically exist, all the orbitals should be considered to accurately compute E_c^{RPA}. However, evaluating expressions for an infinite number of orbitals is not possible in a practical computational setting. In practical implementations, E_{cut}^{χ} is evaluated at different orbital cutoff energies, and is extrapolated to an infinite orbital cut-off energy using

$$E_c^{RPA}\left(E_{cut}^{\chi}\right) = E_c^{RPA}(\infty) + \frac{A}{{E_{cut}^{\chi}}^{\frac{2}{3}}} \quad (13)$$

Even though E_c^{RPA} is extrapolated to infinite orbital cut-off energy, extrapolations based on higher E_{cut}^{χ} values improve the accuracy. At the same time, a higher E_{cut}^{χ} significantly increases the cost of calculations and in many cases makes the modeling of extended, periodic systems unfeasible. $E_{cut}^{\chi} = 200\ eV$ was chosen in this work. To model the extended system, a k-point mesh is required, but the number of k-points included in the computational modeling is directly related to the

computational cost. Especially for RPA calculations with high cutoff energy, employing a dense k-point mesh can be computationally prohibitive. Therefore, we implemented a k-space ONIOM like scheme[34,35] to describe the energetics. For the (3×2) surface models, the energy is calculated using:

$$E^{RPA}(200\,eV, 4\times 6\times 1) =$$

$$E^{RPA}(200\,eV, 3\times 4\times 1) + E^{RPA}(100\,eV, 4\times 6\times 1) - E^{RPA}(100\,eV, 3\times 4\times 1) \quad (14)$$

2.5. Computational setup. All calculations in this paper were carried out using the Vienna Ab-Initio Simulation Package (VASP)[49]. The DFT calculations utilized a plane-wave basis set with a cutoff energy of 550 eV. Core electrons were treated with the projector augmented wave (PAW) method[50]. *GW* pseudopotentials were used for all calculations. Second order Methfessel-Paxton smearing with sigma value of 0.2 eV was used for all DFT slab optimizations and gaussian smearing with sigma value of 0.05 eV was used for molecular references.

The slab calculations were conducted in a 3×2 unit cell of a three-layer slab for non-SC calculations. We use the experimental lattice constant of 3.615Å for PBE, RPBE and RPA[15]. This selection allows RPA calculations to utilize PBE-optimized structures. Repeated images of the slabs are separated by 15 Å. Dipole corrections were applied during the DFT calculations. During optimization, the bottom layer of Cu atoms was kept fixed, while the top two layers were allowed to relax. A (6×8×1) k-point mesh was used. Structural convergence was achieved when forces were below 0.01 eV/Å. The implicit solvation effects were described using the VASPsol package[29], which implements the linearized Poisson Boltzmann model. The dielectric constant of water, 78.4, and the Debye screening length corresponding to 1 M concentration of electrolytes, 3.0 Å were used. We chose the dielectric constant of bulk water, though the dielectric constant near a metal surface is likely much lower. However, the previous benchmarks show that dielectric constant has a minimal impact on the adsorption energy[51,52]. A (8×8×1) k-point mesh was used for DOS calculations, and the convergence test can be seen in Figure S4.

For all DFT methods, the energy of molecular reference energies (CO, H_2 and H_2O) were calculated using a 15×16×17 Å^3 supercell to suppress the spurious interactions between periodic images. RPA calculations are based on optimized PBE structures, and the values were extrapolated to the isolated molecule limit based on a series of calculations with different box sizes (7×8×9 Å^3, 8×9×10 Å^3, 9×10×11 Å^3, and 10×11×12Å^3 for E_{cut}^{χ} = 200 eV and 250 eV, and additional 11×12×13 Å^3 for E_{cut}^{χ} =100 eV and 150 eV). Molecular calculations were performed with a Γ point only k-point mesh.

The adsorption internal energy of *OH at *pzc* is calculated as:

$$E_{ads} = E_{slab+OH} - E_{slab} - (E_{H2O} - \frac{1}{2}E_{H2}) \quad (15)$$

The potential-dependent adsorption free energy of *OH is calculated as:

$$\Omega_{ads}(U) = \Omega_{slab+OH}(U) - \Omega_{slab}(U) - G_{H2O} + (\frac{1}{2}G_{H2} - eU_{SHE} - k_B T ln10 pH) \quad (16)$$

The vibrational frequencies were calculated within the harmonic approximation using the PBE functional and frequencies below 50 cm^{-1} were reset to 50 cm^{-1}. The calculated electronic energies were converted into free energies as follows: for surface species, only vibrational entropies were accounted for, while for gas phase molecules, both translational and rotational entropies were included in addition to vibrational contributions. The fugacity values of gas molecules are taken from Ref[53].

3. Results and Discussion

3.1. *OH adsorption at potential of zero charge (*pzc*). We first used RPA-sol to characterize site dependent adsorption on Cu(100) at the *pzc* without including explicit potential effects. Table 1 summarizes adsorption internal energies for *OH and *CO computed with PBE, RPBE, and RPA. For *OH, the on top configuration is intrinsically unstable on Cu(100) indicating the preference of *OH to form multiple Cu-O interactions. In practice, structural relaxation with RPBE does not preserve an on top minimum but diffuses to a bridge like mode; we therefore report no RPBE on top value. At the *pzc*, both semi-local GGA functionals and RPA identify the hollow site as the most stable adsorption site, but they differ markedly in the predicted binding strength. RPBE gives positive therefore weak OH adsorption energies of 0.354 eV and 0.340 eV for the bridge and hollow sites, respectively, markedly weaker than the stabilization predicted by RPA (-0.193 and -0.05 eV respectively). PBE is generally closer to RPA for the on top and bridge geometries, yet it still underestimates the stability of the hollow site, yielding -0.011 eV compared with -0.193 eV from RPA. Overall, both PBE and RPBE underestimate *OH stabilization on Cu(100), with the error being considerably larger for RPBE.

For *CO, PBE and RPBE both favor bridge adsorption, whereas RPA stabilizes on top CO, consistent with the well-known sensitivity of CO chemisorption to the electronic structure treatment. In addition, the magnitude of the CO binding energy is strongly functional dependent. PBE overbinds CO relative to RPA by about 0.3 eV on the on top site and by roughly 0.45 to 0.57 eV for bridge and hollow adsorption, while RPBE is much closer to RPA for on-top CO and only modestly overbinds at bridge and hollow sites. The contrasting trends for *OH and *CO highlight that the apparent “best” GGA functional is adsorbate dependent: RPBE improves *CO energetics relative to PBE but simultaneously degrades *OH a marked underestimation of the adsorption energy. Thus, the performance of a given GGA functional is not systematic across adsorbates: the same functional can underbind one intermediate while overbinding another, making it difficult to select a single “best” semi-local functional for chemically complex electrochemical interfaces with both CO and OH adsorbates where relative stabilities rather than absolute energies control the surface state.

Table 1. Comparison of the adsorption internal energy of *OH and *CO using DFT-GGA functionals PBE, RPBE and RPA.

Adsorbate	site	PBE (eV)	RPBE (eV)	RPA (eV)
*OH	*top*	0.592	—	0.584
	bridge	0.060	0.354	-0.050
	hollow	-0.011	0.340	-0.193
*CO	*top*	-0.859	-0.558	-0.565
	bridge	-0.897	-0.562	-0.440
	hollow	-0.867	-0.543	-0.300

We also evaluated *OH adsorption on representative defective motifs to probe how local structure controls *OH binding. Starting from a Cu(100) (3 × 2) slab, we constructed three defect families: a single surface vacancy, denoted (3 × 2)-v; a single adatom, denoted (3 × 2)-ad; and an adatom dimer, denoted (3 × 2)-ad-di (Figure 1a). These models generate a range of terrace-like and undercoordinated environments. Adsorption sites were grouped into top, bridge, and hollow motifs, and the adsorption energies were analyzed as a function of the average coordination number (CN) of the Cu atoms directly involved in bonding. We emphasize that those defective structures are not intended to represent an equilibrium surface phase diagram. Instead, they serve as representative low-coordination Cu environments that allow us to isolate how local geometric structure influences *OH adsorption, while the thermodynamic formation and population of such motifs under electrochemical conditions remain beyond the scope of the present study. The defective models considered here should be viewed as physically motivated local environments that may become accessible under reaction conditions, rather than as uniquely identified dominant surface states.

For top sites, *OH binding strengthens as CN decreases (Figure 1b). PBE and RPA follow similar trends, whereas RPBE systematically predicts weaker binding. Notably, even at the most undercoordinated adatom top site, *OH remains only weakly stabilized and can be thermodynamically unfavorable, consistent with the preference of *OH for forming multiple Cu-O bonds rather than a single on-top bond. For bridge sites (Figure 1b), the adsorption energy does not exhibit a simple linear dependence on CN. Compared to planar and vacancy-adjacent bridge motifs, bridge adsorption involving adatoms is less stabilizing, particularly for asymmetric bridges between an adatom and a terrace Cu atom. This behavior indicates that bridge stability is controlled not only by the mean coordination but also by bond asymmetry and the local geometric constraint imposed by dissimilar Cu environments. In contrast, the adatom dimer provides a more symmetric, undercoordinated bridge motif that can strongly bind *OH, with RPA adsorption energies reaching approximately -0.5 eV, suggesting that such undercoordinated paired sites can act as traps for *OH. The extra-stabilization for OH compared to the pristine Cu(100) surface (ca 0.3 eV) is however not strong enough to promote a restructuring of the planar surface. For hollow sites (Figure 1b), the trend is reversed relative to the naive expectation from averaged CN and the highly-coordinated pristine Cu(100) proposes the most stable hollow site. The threefold hollow motif formed by an adatom and two terrace Cu atoms is not particularly favorable for *OH, even though its average CN is lower than that of the fourfold terrace hollow site. This indicates that the identity of the

specific Cu atoms involved matters more than the averaged descriptor. In particular, when one or more participating Cu atoms are highly coordinated, their contribution to Cu-O bonding is weaker, and the resulting adsorption resembles an effectively on-top interaction on the remaining undercoordinated Cu. Consistent with this picture, the same structure also yields unfavorable adsorption at the corresponding asymmetric bridge motif, reinforcing that *OH adsorption is penalized when bonding is dominated by an asymmetric environment that mixes highly coordinated and undercoordinated Cu atoms.

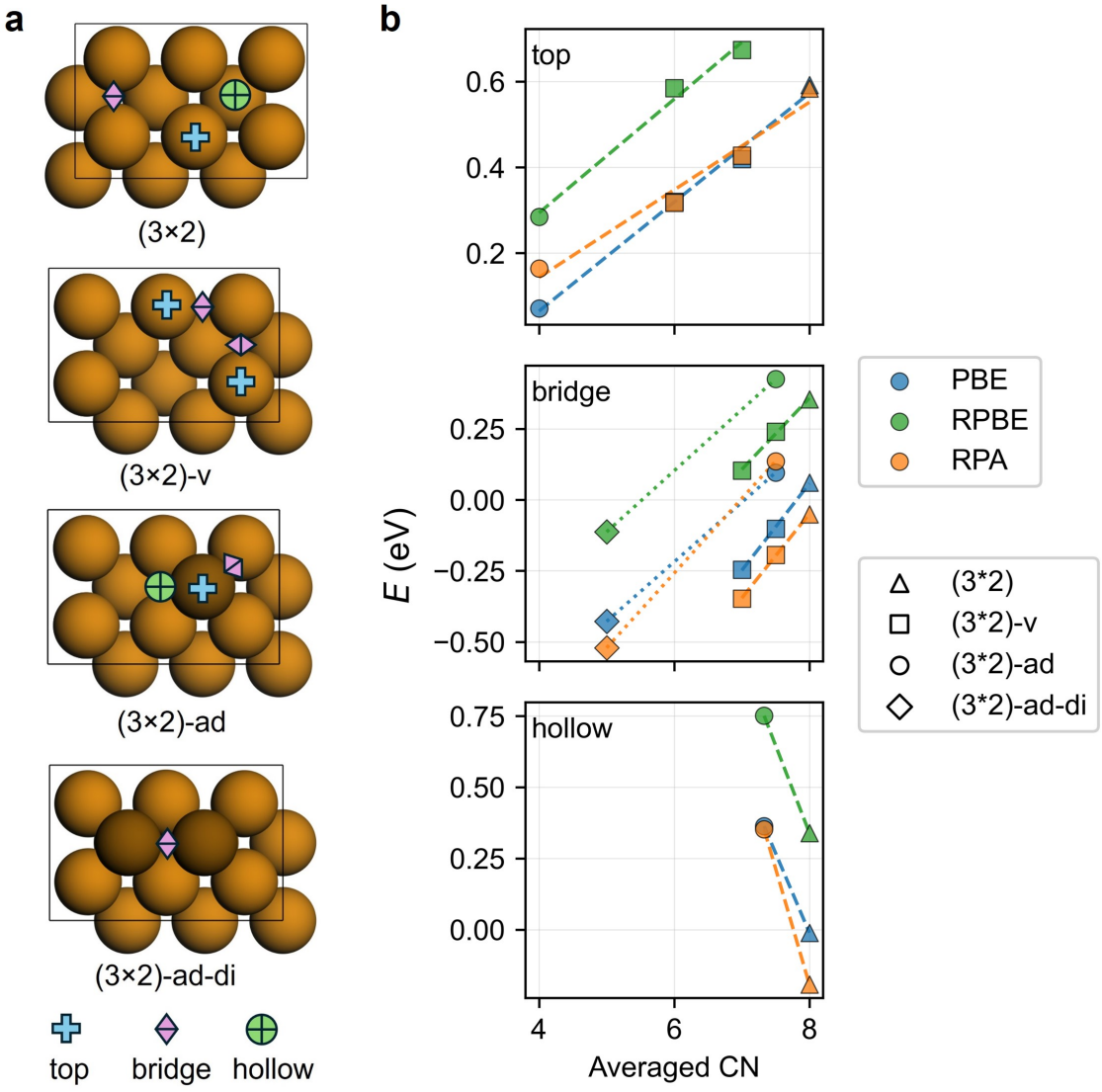

Figure 1. (a) Atomic models of (3*2) Cu(100) surfaces with one vacancy [(3*2)-v], one adatom [(3*2)-ad] and adatom-dimer [(3*2)-ad-di]. Triangle, square and circle labels represent top, bridge and hollow sites, respectively. (b) Adsorption internal energy of *OH on various sites as a function of coordination number (CN) using RPA and DFT-PBE/RPBE functionals.

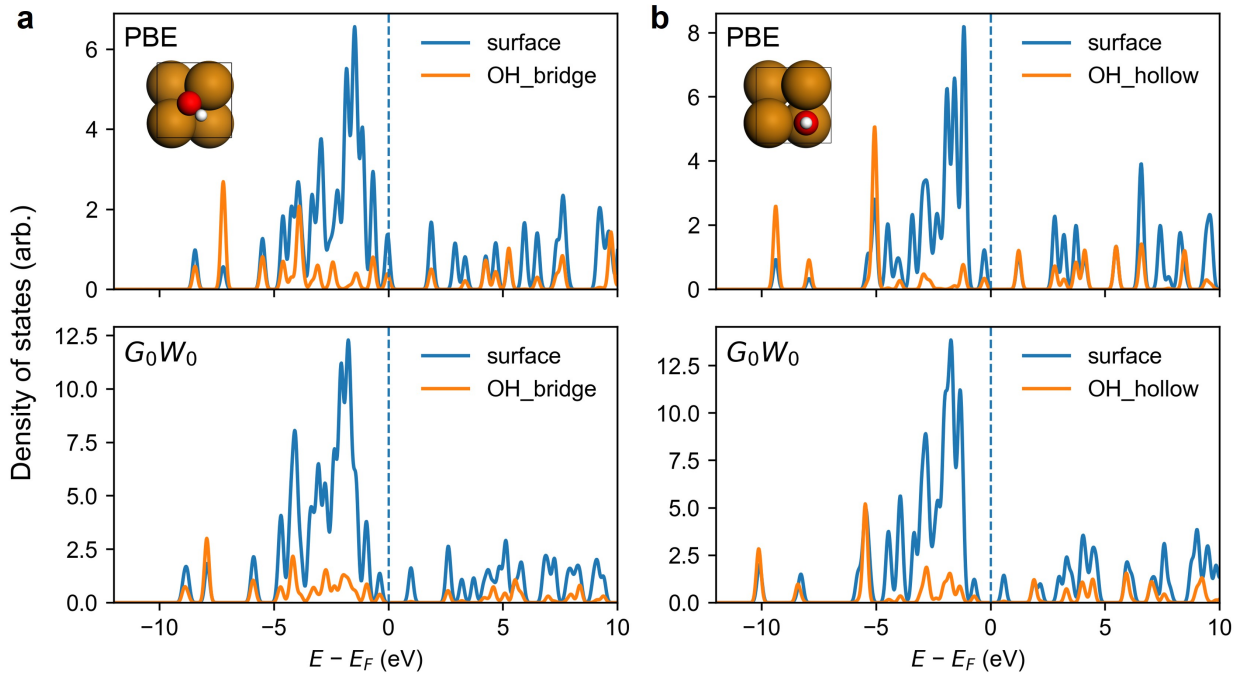

Figure 2. Electronic DOS for OH adsorbed (a) on bridge site (b) on hollow site on $\sqrt{3} \times \sqrt{3}$ Cu(100) evaluated using DFT (PBE) and RPA (G_0W_0).

We will now discuss the electronic origin of the adsorption energy difference between RPA and DFT-PBE. For that purpose, one can calculate the quasiparticle energies using the GW method in the RPA approximation, an approach compatible with RPA energies. The density of states (DOS) in Figure 2 reveals clear quasiparticle-level modifications of the Cu-OH electronic structure when going from DFT-PBE to G_0W_0. First, the three prominent OH-derived occupied peaks below -5 eV (-5 to -6 eV, ~-7 eV, and ~-8 to -9 eV in PBE) shift to more negative energies in G_0W_0, indicating stabilization of bonding states. Second, in PBE a finite OH-related feature appears very close to the Fermi level, and in bridge-site case (Figure 2a) crosses E_F, suggesting incomplete separation between bonding and antibonding manifolds. In G_0W_0, this near-E_F OH weight is clearly reduced. Third, OH-derived unoccupied spectral weight above E_F is displaced to higher energies in G_0W_0, indicating that antibonding states are pushed upward. As a result, the energetic separation between the occupied bonding and the unoccupied antibonding becomes larger in G_0W_0 than in PBE, reflecting an increased bonding-antibonding splitting in the many-body description.

These electronic changes are accompanied by stronger Cu-OH hybridization below E_F, particularly at the hollow site. In G_0W_0, the surface Cu DOS more fully overlaps the OH bonding peaks in the -8 to -4 eV region compared to PBE, indicating enhanced mixing between adsorbate and surface states. Within a molecular-orbital framework, the deepest peak (-8 to -9 eV) corresponds primarily to σ-type coupling between O lone-pair character and Cu 3d/4s states, while the features in the -6 to -5 eV range arise from π-type interactions involving O 2*p* orbitals and Cu 3*d* states. The Cu *d*-band center shifts to lower energy in the G_0W_0 description compared to DFT-PBE, moving from -2.571 to -2.963 eV for the bridge site and from -2.581 to -2.935 eV for the

hollow site (Figure 2b), which further reflects a many-body renormalization of the surface electronic structure that favors stronger adsorbate-metal coupling. Together, the deepening of bonding states, upward displacement of antibonding states, and enhanced occupied-state hybridization provide a consistent electronic-structure explanation for the stronger OH adsorption predicted by RPA, especially at the hollow site.

3.2. Potential-dependent *OH adsorption. We next consider potential-dependent *OH adsorption and compare directly with electrochemical cyclic voltammetry (CV) fingerprints, which provide an unusually stringent benchmark for an otherwise reactive adsorbate. A common starting point for potential effects is the CHE model[46], which captures the leading thermodynamic dependence on electrode potential but can become unreliable when explicit surface charging, charge transfer, or double-layer polarization contributes appreciably. A constant-potential description based on a GC treatment of electrons is therefore more appropriate for adsorption at electrified interfaces. In this work, we employ two constant-potential strategies as discussed in the Method section. The first is a fully GC implementation of RPA (GC-RPA) that treats the electrode potential explicitly, but the computational cost restricts calculations to small surface cells and can enforce unrealistically high coverages. The second combines GC-DFT with RPA ground-state energetics through an extrapolation procedure, which enables larger cells and lower coverages. Because this extrapolation is an approximation that the potential dependence is the same between GCDFT and GCRPA, its reliability must be established before applying it broadly.

We therefore use a Cu(100) $\sqrt{3} \times \sqrt{3}$ surface cell with *OH adsorbed at bridge and hollow sites as a representative test case. The grand-canonical formalism is the same for GC-DFT and GC-RPA; the practical difference lies in how the Fermi level, ε_F, is obtained. In standard GC-DFT, ε_F is taken directly from the self-consistent electronic structure calculation, whereas in GC-RPA such a self-consistent ε_F is not available and must instead be obtained from the derivative of the total energy with respect to the number of electrons, referred to here as the "Energetic" approach. This energetic procedure can also be applied at the DFT-PBE level and therefore provides a useful internal benchmark. Figure 3a compares the ε_F obtained from a self-consistent DFT-PBE calculation (GCDFT-PBE-SCF) with those extracted from an energy-based approach for both DFT-PBE (GCDFT-PBE-Energetic) and RPA (GC-RPA-Energetic) as the surface charge is varied. At the DFT-PBE level, the energy-based ε_F closely matches the self-consistent values, indicating that the energy-based procedure provides a reliable route to the electron chemical potential when a self-consistent ε_F is not available. In contrast, the ε_F obtained from the RPA energy-based analysis differ substantially from DFT-PBE, highlighting that using the Hartree–Fock reference step to infer the chemical potential of electron can be inaccurate and motivating the energy-based treatment within the GC-RPA framework.

Using the resulting ε_F , we calculated grand-canonical adsorption free energies as functions of electrode potential (Figure 3b). At the DFT-PBE level, grand-canonical energies derived from the self-consistent and energy-based approaches are essentially identical over the relevant potential

window, consistent with the agreement in their ε_F. This benchmark indicates that the energetic procedure provides a reliable route to the electron chemical potential when a self-consistent ε_F is not available, as in the GC-RPA framework. Comparing DFT-PBE and RPA, *OH adsorption is systematically stabilized by RPA for both bridge and hollow sites, in line with the stronger binding already observed at the *pzc*. The constant-potential treatment further reveals a site-stability crossover that depends sensitively on the electronic-structure method. While the hollow site is preferred near the *pzc*, GC-DFT-PBE predicts that the bridge site becomes more stable at potentials more negative than about −0.50 V vs SHE. In contrast, GC-RPA shifts this crossover to significantly more negative potentials, around −1.05 V vs SHE, because RPA preferentially stabilizes hollow-bound *OH. This qualitative difference cannot be captured by a simple CHE picture.

Importantly, the computed grand-canonical adsorption energies are close to linear functions of electrode potential for both GC-DFT-PBE and GC-RPA in this regime, indicating that second-order charging contributions are small and that the differential capacitance does not change dramatically upon adsorption. In particular, the slopes of the potential dependence ($\partial\Delta\Omega/\partial U$) are similar at the GC-DFT-PBE and GC-RPA levels, supporting the central assumption of the extrapolation strategy: GC-DFT captures the leading potential dependence, while RPA provides a more accurate description of the adsorption energetics. On this basis, we approximate the potential-dependent RPA adsorption free energy by combining the ground-state RPA adsorption energy with the configuration-specific charging contribution obtained from GC-DFT.

We emphasize that this extrapolation is a benchmarked approximation rather than a formally exact replacement for full GC-RPA. It is expected to be most reliable when the interfacial charging response varies smoothly with potential and when the many-body correction does not strongly alter the capacitance or dipole response of the interface. For the OH/Cu(100) systems considered here, however, the agreement between GC-DFT and GC-RPA slopes supports the use of this approach and enables larger surface cells to be treated at the RPA level, thereby reducing spurious adsorbate-adsorbate interactions associated with artificially high coverages.

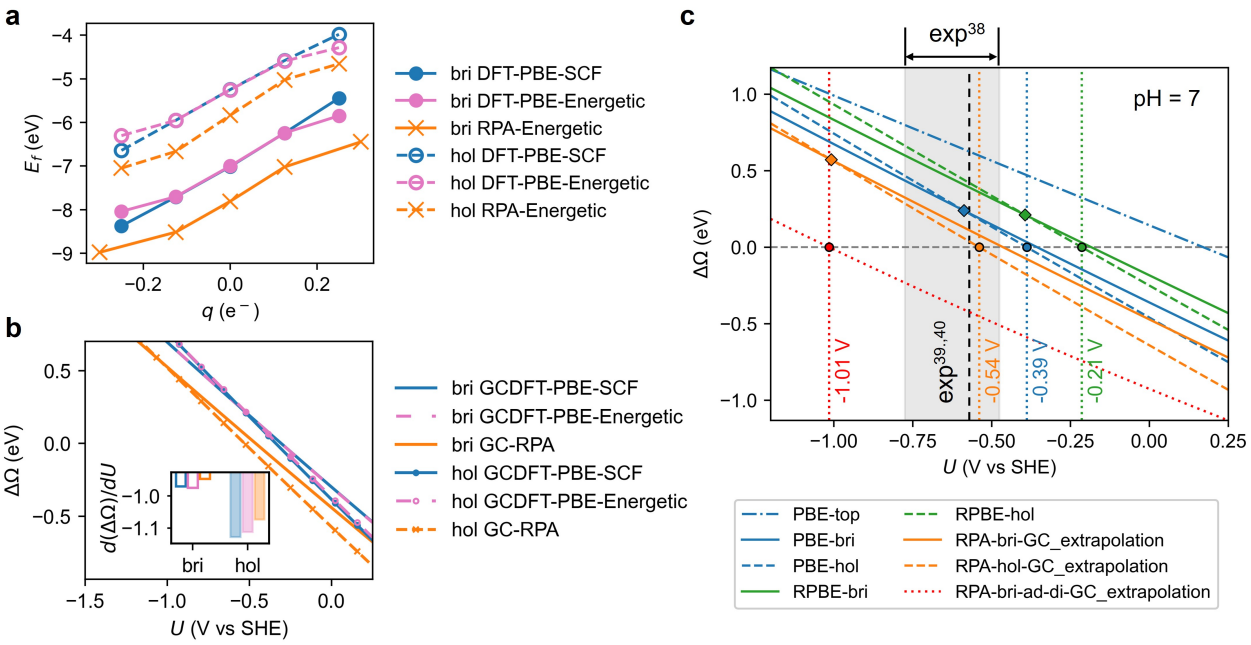

Figure 3. (a) Fermi level (ε_F), as a function of surface charge for the $\sqrt{3} \times \sqrt{3}$ Cu(100) surface with *OH, comparing values taken directly from the self-consistent DFT-PBE electronic structure ("GCDFT-PBE-SCF") with those obtained from the energy-derivative approach at the DFT-PBE ("GCDFT-PBE-Energetic") and RPA ("GC-RPA-Energetic") levels. (b) Grand canonical free energy of *OH adsorption calculated with the 'Energetic' approach compared with the results from the SCF approach in the case of PBE (lines overlap). The inset shows the first derivative of grand canonical energy versus electrode potential $d\Delta\Omega/dU$ on bridge and hollow sites. (c) Potential-dependent *OH adsorption free energy on selected surface sites, computed with GC-DFT-GGA (PBE, RPBE) and RPA based on GC-DFT extrapolation at pH=7 on Cu (3 × 2) surface cell. Circles and vertical dashed lines denote the potentials at which ΔΩ(*OH) = 0, corresponding to the onset of thermodynamic stability. Diamonds indicate the crossover potentials where *OH adsorption free energy at bridge sites equals that at hollow sites.

Since GC extrapolation based on RPA ground state energies provides a reliable route for incorporating potential effects, we next apply this approach to a Cu(100) (3 × 2) surface cell and evaluate potential dependent *OH adsorption on bridge and hollow sites (Figure 3c). We focus on the condition ΔΩ(*OH) = 0, which defines the desorption potential and can be compared directly with CV fingerprints. For PBE and RPBE, the predicted desorption potentials are -0.39 V and -0.21 V vs SHE, respectively, indicating substantially reduced *OH stability. In contrast, RPA predicts a desorption potential of -0.54 V vs SHE, in excellent agreement with the experimental value of approximately -0.56 V vs SHE at pH 7[39,40]. To our knowledge, this provides the first direct many body quantification of an OH adsorption/desorption potential under electrochemical conditions.

Consistent with the fully GC analysis, RPA GC extrapolation also shifts the bridge-hollow site stability crossover to more negative potentials, reflecting the preferential stabilization of hollow

bound *OH. We note, however, that the (3 × 2) cell necessarily describes isolated adsorption and does not capture the possibility of hydrogen bonded *OH networks, which may further stabilize bridge site *OH at higher coverages. Finally, motivated by operando observations that Cu surfaces restructure under cathodic conditions and generate undercoordinated motifs, we evaluate *OH stability on representative low coordination defects. On an adatom dimer motif, RPA predicts a substantially extended stability window, with the desorption potential shifting to approximately -1.01 V vs SHE at pH 7. This stronger stabilization at undercoordinated sites provides a plausible thermodynamic basis for the persistence of OH related signatures detected by in situ Raman spectroscopy at strongly negative potentials[41].

3.3. Surface landscape of CO and OH co-adsorption. CO chemisorption on transition-metal surfaces is notoriously sensitive to the electronic-structure treatment, as highlighted by the well-known "CO puzzle," and Cu is no exception. Above we further show that commonly used GGA functionals, including PBE and RPBE, also exhibit substantial and adsorbate-dependent errors for OH adsorption on Cu(100). This inconsistency becomes particularly problematic under CO_2RR-relevant conditions, where experiments indicate that *CO and *OH can coexist on the surface over a broad potential window[41,42]. In practice, RPBE often yields CO binding energies closer to many-body benchmarks than PBE, yet it simultaneously underestimates ∗OH stability; consequently, a functional that appears reasonable for *CO can fail for *OH and misrepresent the thermodynamics of co-adsorption. Motivated by this, we rechart the surface landscape of Cu(100) in a (3 × 2) cell under combined *CO/*OH adsorption, with an explicit focus on how many-body energetics reshape relative stabilities and phase boundaries. To incorporate electrode-potential effects at tractable cost, we employ the RPA GC extrapolation scheme developed above rather than a fully GC-RPA treatment, which remains computationally prohibitive for the larger cells required to avoid artificial high-coverage interactions. Note that the corresponding changes in surface dipole and work function are included self-consistently for each configuration.

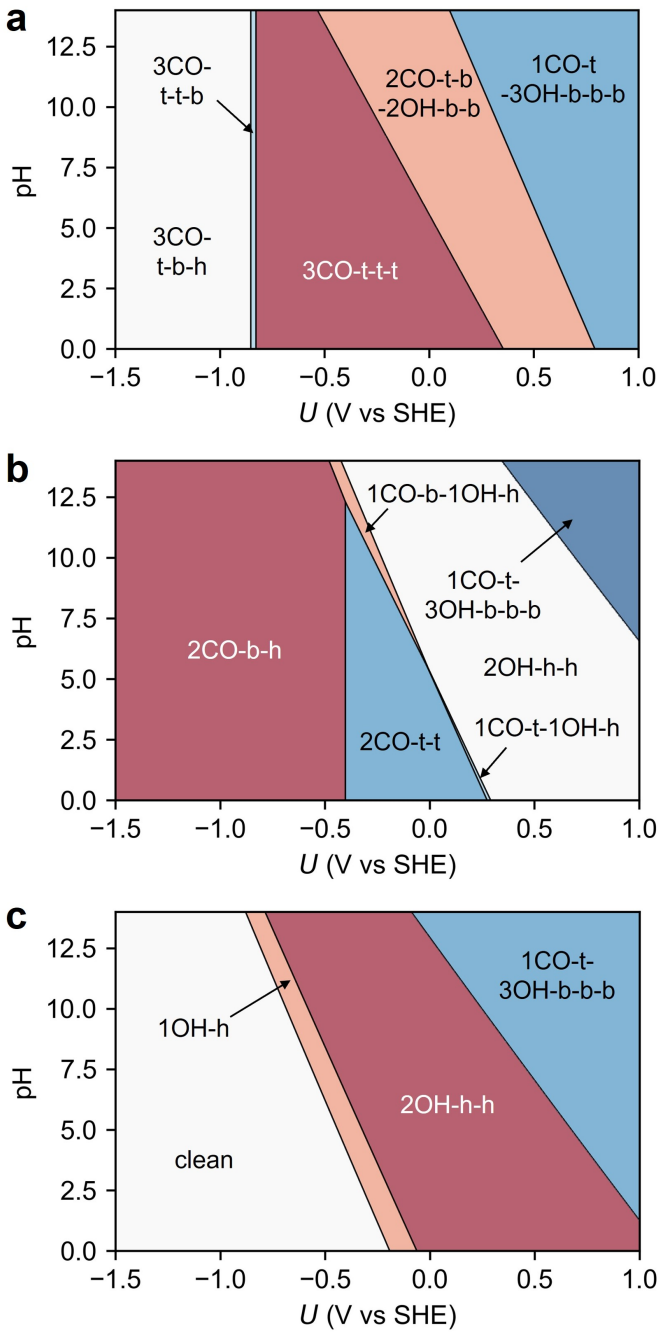

Figure 4. Pourbaix diagram for co-adsorbed OH and CO on Cu(100) (3*2) unit cell as functions of electrode potential and pH using (a) DFT-PBE functional (b) DFT-RPBE functional and (c) RPA. The partial pressure of CO is set as 0.05 atom, corresponding to the typical CO_2RR conditions. The labels, t, b, h represent top, bridge and hollow sites respectively.

For the PBE functional, the surface is dominated by a high CO coverage across most of the potential–pH window (Figure 4a). A broad region with three *CO adsorbed at on-top sites persists from moderately negative potentials to near zero bias, and only at sufficiently positive potentials

does a mixed *CO/*OH phase (one *CO with three *OH) become competitive. An intermediate region containing two *CO and two *OH appears only as a narrow wedge, indicating that within PBE the surface thermodynamics are largely governed by strong CO stabilization, with *OH becoming prominent mainly under the most oxidizing conditions. RPBE exhibits a similar qualitative progression but with reduced CO coverage relative to PBE (Figure 4b). The negative-potential region remains CO covered, yet phases containing fewer *CO and increasing *OH content occupy a larger fraction of the diagram at more positive potentials, including mixed states with one *CO and one to two *OH as well as the *CO + 3*OH phase, depending on pH and potential.

RPA yields a markedly different surface landscape (Figure 4c). At negative potentials, a wide region of the diagram corresponds to clean Cu(100), consistent with the unfavorable CO adsorption under cathodic bias reported in our previous work[51]. In moderate potentials, the stable phases are hydroxyl rich (one *OH or two *OH at hollow sites) without concomitant *CO adsorption, reflecting the stronger *OH affinity predicted by the many-body treatment. *CO becomes competitive only at sufficiently positive potentials, where the mixed *CO + 3*OH phase is stabilized. Overall, RPA differs from semi-local DFT in that it stabilizes *OH substantially and therefore predicts a much wider potential window for *OH persistence, whereas both PBE and RPBE favor CO-covered states, albeit for different reasons: PBE tends to overbind *CO, while RPBE destabilizes *OH. Finally, we note that these Pourbaix maps are constructed in a relatively small surface cell, which limits the diversity of adsorption patterns and may exclude additional low-energy surface states. Extending this analysis to larger supercells would be valuable for a more complete surface-state landscape; while direct sampling at many-body accuracy is currently cost prohibitive, combining many-body calculations with machine-learning approaches offers a promising route[54] and is the subject of ongoing work.

Recent work has proposed that under mild potentials relevant to CORR, coadsorption of *CO and *OH can promote surface restructuring[41]. Grand-canonical sampling identifies a family of metastable motifs in which a Cu atom is lifted from the surface and coordinated by one *CO and two or three *OH groups, denoted $Cu(CO)(OH)_n$ (n = 2 or 3), and these species were suggested as precursors to larger clusters (Figure 5a, b). At the RPBE level, ensemble analysis indicates that such motifs are not the dominant surface state but can appear as metastable configurations[41]. Motivated by our finding that semi-local functionals show inconsistent accuracy for *CO and *OH adsorption, we thus re-evaluate the thermodynamic stability of these $Cu(CO)(OH)_n$ complexes using RPA.

Figure 5c shows that the predicted stability window of $Cu(CO)(OH)_n$ is strongly functional dependent. Using RPBE, the complex becomes stable only at potentials more positive than approximately -0.09 V vs SHE. In contrast, both PBE and RPA stabilize the complex over substantially more cathodic conditions, extending the stability limit to about -0.35 V and -0.32 V vs SHE, respectively. At -0.32 V SHE, the predicted formation energy of $Cu(CO)(OH)_n$ differs by as much as 0.46 eV between RPBE and RPA, indicating that the relative energetic placement of

these metastable reconstructed motifs can shift dramatically depending on the electronic structure treatment. While a full quantitative assessment will ultimately require explicit sampling of reconstructed ensembles and consistent comparison to unreconstructed reference surfaces within the same grand-canonical framework, these results suggest that many-body energetics can materially alter the predicted accessibility of proposed Cu(CO)$(OH)_n$ precursors under reaction conditions.

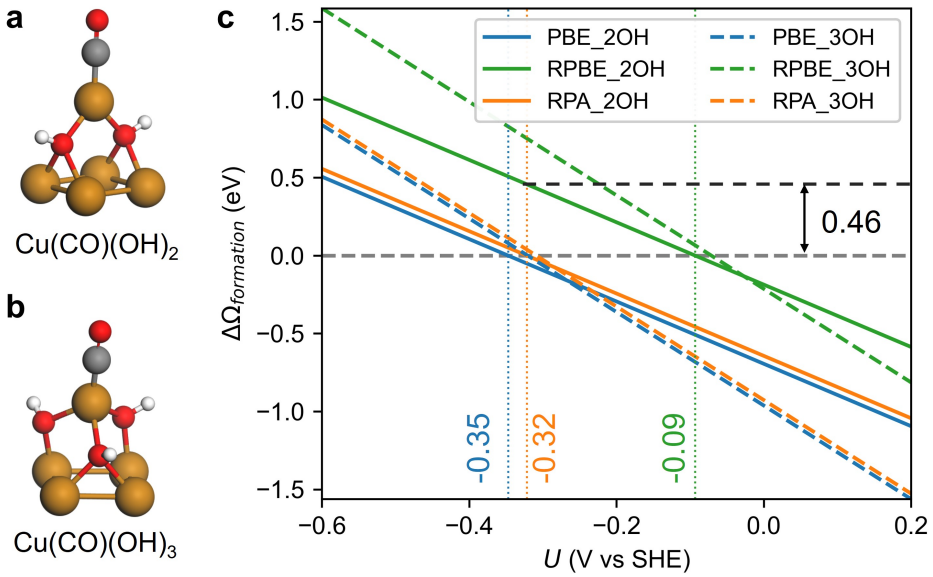

Figure 5. The atomic structure of (a) $Cu(CO)(OH)_2$ and (b) $Cu(CO)(OH)_3$ complex on (3×2) Cu(100) surface. (b) The formation free energy of the complex as the function of electrode potential at pH = 7. The vertical dashed lines denote the potential at which $\Delta\Omega_{formation} = 0$ (onset of thermodynamic stability).

4. Conclusions

In this work, we established a reference-quality description of *OH adsorption on Cu(100) under electrochemical conditions using electrochemical-aware many-body perturbation theory. By combining RPA with implicit solvation (RPA-sol), constant-potential treatments through fully grand-canonical RPA (GC-RPA), and an efficient GC-extrapolation strategy that couples GCDFT with RPA ground-state energetics, we quantified both site-dependent and potential-dependent *OH stability in a unified framework. The GC-extrapolation route was benchmarked against direct GC treatments and shown to capture the leading potential dependence reliably, enabling larger surface cells and reducing artificial adsorbate–adsorbate interactions associated with high coverages within small unit cells.

Electrochemical-aware RPA reproduces the experimental CV fingerprint for *OH adsorption/desorption on Cu(100), yielding an *OH desorption potential of -0.54 V vs SHE in excellent agreement with the experimentally inferred value of -0.56 V vs SHE. In contrast, widely used DFT-GGA functionals underestimate *OH stability and compress the stability window under

reducing conditions, with RPBE showing particularly large errors for *OH even when it improves *CO energetics. The contrasting functional trends for *OH and *CO underscore a central challenge for chemically complex electrochemical interfaces: a single semi-local functional can underbind one adsorbate while overbinding another, biasing predicted surface states and co-adsorption thermodynamics.

Beyond terrace adsorption, *OH binding depends sensitively on local coordination and site symmetry across representative defect motifs. Undercoordinated paired sites can act as *OH traps, extending the predicted stability window to substantially more negative potentials and providing a thermodynamic basis for the persistence of OH-related signatures under strongly cathodic conditions. Electronic-structure analysis at the G_0W_0-RPA level further rationalizes the DFT–RPA discrepancy as a many-body renormalization of the interfacial electronic response that strengthens Cu–OH bonding and increases Cu–OH hybridization, particularly for hollow site adsorption.

Finally, we recharted the Cu(100) surface-state landscape under *CO/*OH co-adsorption and reassessed the stability of proposed $Cu(CO)(OH)_n$ restructuring motifs. The resulting Pourbaix maps and complex-stability windows differ qualitatively between PBE, RPBE, and RPA, illustrating that many-body accuracy can alter phase boundaries, interfacial speciation, and the accessibility of reconstructed motifs under operating conditions.

Overall, these results demonstrate that electrochemical-aware RPA provides a robust and systematically improvable framework for quantitative adsorption thermodynamics under electrochemical conditions. By enabling reliable surface-state predictions for reactive intermediates in solvated, electrified environments, the approach offers a practical route to many-body benchmarks for electrochemical interfaces and a foundation for future studies of co-adsorption, restructuring, and dynamic surface evolution, including extensions to larger configurational spaces through many-body-informed machine learning strategies.

Supporting information: The benchmarks of orbital cutoff energy, k-point mesh, the discussion of coverage and solvent effects and their limitations.

Acknowledgments. The work was supported by the National Science Foundation CBET grant 2103116, the National Science Foundation CDS&E grant 2152767 and the Audi CO_2 Cy Pres Award. D. Cheng is supported by UCLA Dissertation Year Fellowship. Computational resources for this work were provided by the UCLA-shared cluster Hoffman2, and the Expanse cluster through the allocation CHE170060 at the San Diego Supercomputing Center through ACCESS.

Conflict of Interest. The authors declare no conflict of interest.

References

(1) Ertl, G. Elementary Steps in Heterogeneous Catalysis. *Angew. Chem. Int. Ed. Engl.* **1990**, *29* (11), 1219–1227. https://doi.org/10.1002/anie.199012191.
(2) Perdew, J. P.; Burke, K.; Ernzerhof, M. Generalized Gradient Approximation Made Simple. *Phys. Rev. Lett.* **1996**, *77* (18), 3865–3868. https://doi.org/10.1103/PhysRevLett.77.3865.
(3) Perdew, J. P.; Chevary, J. A.; Vosko, S. H.; Jackson, K. A.; Pederson, M. R.; Singh, D. J.; Fiolhais, C. Atoms, Molecules, Solids, and Surfaces: Applications of the Generalized Gradient Approximation for Exchange and Correlation. *Phys. Rev. B* **1992**, *46* (11), 6671–6687. https://doi.org/10.1103/PhysRevB.46.6671.
(4) Wichtendahl, R.; Rodriguez-Rodrigo, M.; Härtel, U.; Kuhlenbeck, H.; Freund, H.-J. Thermodesorption of CO and NO from Vacuum-Cleaved NiO(100) and MgO(100). *Phys. Status Solidi A* **1999**, *173* (1), 93–100. https://doi.org/10.1002/(SICI)1521-396X(199905)173:1%253C93::AID-PSSA93%253E3.0.CO;2-4.
(5) Campbell, C. T.; Sellers, J. R. V. Enthalpies and Entropies of Adsorption on Well-Defined Oxide Surfaces: Experimental Measurements. *Chem. Rev.* **2013**, *113* (6), 4106–4135. https://doi.org/10.1021/cr300329s.
(6) Tait, S. L.; Dohnálek, Z.; Campbell, C. T.; Kay, B. D. N -Alkanes on MgO(100). I. Coverage-Dependent Desorption Kinetics of n-Butane. *J. Chem. Phys.* **2005**, *122* (16), 164707. https://doi.org/10.1063/1.1883629.
(7) Miller, J. B.; Siddiqui, H. R.; Gates, S. M.; Russell, J. N.; Yates, J. T.; Tully, J. C.; Cardillo, M. J. Extraction of Kinetic Parameters in Temperature Programmed Desorption: A Comparison of Methods. *J. Chem. Phys.* **1987**, *87* (11), 6725–6732. https://doi.org/10.1063/1.453409.
(8) Spoto, G.; Gribov, E.; Damin, A.; Ricchiardi, G.; Zecchina, A. The IR Spectra of Mg5C2+(CO) Complexes on the (001) Surfaces of Polycrystalline and Single Crystal MgO. *Surf. Sci.* **2003**, *540* (2–3), L605–L610. https://doi.org/10.1016/S0039-6028(03)00830-6.
(9) Goyhenex, C.; Croci, M.; Claeys, C.; Henry, C. R. FTIR Studies of the Adsorption of CO on Supported Metallic Clusters. *Surf. Sci.* **1996**, *352–354*, 475–479. https://doi.org/10.1016/0039-6028(95)01182-X.
(10) Campbell, C. T.; Lytken, O. Experimental Measurements of the Energetics of Surface Reactions. *Surf. Sci.* **2009**, *603* (10–12), 1365–1372. https://doi.org/10.1016/j.susc.2008.08.028.
(11) Tchakoua, T.; Gerrits, N.; Smeets, E. W. F.; Kroes, G.-J. SBH17: Benchmark Database of Barrier Heights for Dissociative Chemisorption on Transition Metal Surfaces. *J. Chem. Theory Comput.* **2023**, *19* (1), 245–270. https://doi.org/10.1021/acs.jctc.2c00824.
(12) Sauer, J. Ab Initio Calculations for Molecule–Surface Interactions with Chemical Accuracy. *Acc. Chem. Res.* **2019**, *52* (12), 3502–3510. https://doi.org/10.1021/acs.accounts.9b00506.
(13) Zhao, Y.; Truhlar, D. G. Design of Density Functionals That Are Broadly Accurate for Thermochemistry, Thermochemical Kinetics, and Nonbonded Interactions. *J. Phys. Chem. A* **2005**, *109* (25), 5656–5667. https://doi.org/10.1021/jp050536c.
(14) Mallikarjun Sharada, S.; Bligaard, T.; Luntz, A. C.; Kroes, G.-J.; Nørskov, J. K. SBH10: A Benchmark Database of Barrier Heights on Transition Metal Surfaces. *J. Phys. Chem. C* **2017**, *121* (36), 19807–19815. https://doi.org/10.1021/acs.jpcc.7b05677.
(15) Schimka, L.; Harl, J.; Stroppa, A.; Grüneis, A.; Marsman, M.; Mittendorfer, F.; Kresse, G. Accurate Surface and Adsorption Energies from Many-Body Perturbation Theory. *Nat. Mater.* **2010**, *9* (9), 741–744. https://doi.org/10.1038/nmat2806.

(16) Shi, B. X.; Zen, A.; Kapil, V.; Nagy, P. R.; Grüneis, A.; Michaelides, A. Many-Body Methods for Surface Chemistry Come of Age: Achieving Consensus with Experiments. *J. Am. Chem. Soc.* **2023**, *145* (46), 25372–25381. https://doi.org/10.1021/jacs.3c09616.
(17) Gil, A. Site Preference of CO Chemisorbed on Pt(111) from Density Functional Calculations. *Surf. Sci.* **2003**, *530* (1–2), 71–87. https://doi.org/10.1016/S0039-6028(03)00307-8.
(18) Feibelman, P. J.; Hammer, B.; Nørskov, J. K.; Wagner, F.; Scheffler, M.; Stumpf, R.; Watwe, R.; Dumesic, J. The CO/Pt(111) Puzzle. *J. Phys. Chem. B* **2001**, *105* (18), 4018–4025. https://doi.org/10.1021/jp002302t.
(19) Urban, M.; Noga, J.; Cole, S. J.; Bartlett, R. J. Towards a Full CCSDT Model for Electron Correlation. *J. Chem. Phys.* **1985**, *83* (8), 4041–4046. https://doi.org/10.1063/1.449067.
(20) Raghavachari, K.; Trucks, G. W.; Pople, J. A.; Head-Gordon, M. A Fifth-Order Perturbation Comparison of Electron Correlation Theories. *Chem. Phys. Lett.* **1989**, *157* (6), 479–483. https://doi.org/10.1016/S0009-2614(89)87395-6.
(21) Sparta, M.; Neese, F. Chemical Applications Carried out by Local Pair Natural Orbital Based Coupled-Cluster Methods. *Chem Soc Rev* **2014**, *43* (14), 5032–5041. https://doi.org/10.1039/C4CS00050A.
(22) Mostaani, E.; Drummond, N. D.; Fal'ko, V. I. Quantum Monte Carlo Calculation of the Binding Energy of Bilayer Graphene. *Phys. Rev. Lett.* **2015**, *115* (11), 115501. https://doi.org/10.1103/PhysRevLett.115.115501.
(23) Austin, B. M.; Zubarev, D. Yu.; Lester, W. A. Quantum Monte Carlo and Related Approaches. *Chem. Rev.* **2012**, *112* (1), 263–288. https://doi.org/10.1021/cr2001564.
(24) Foulkes, W. M. C.; Mitas, L.; Needs, R. J.; Rajagopal, G. Quantum Monte Carlo Simulations of Solids. *Rev. Mod. Phys.* **2001**, *73* (1), 33–83. https://doi.org/10.1103/RevModPhys.73.33.
(25) Sparta, M.; Neese, F. Chemical Applications Carried out by Local Pair Natural Orbital Based Coupled-Cluster Methods. *Chem Soc Rev* **2014**, *43* (14), 5032–5041. https://doi.org/10.1039/C4CS00050A.
(26) Steinmann, S. N.; Michel, C.; Schwiedernoch, R.; Sautet, P. Impacts of Electrode Potentials and Solvents on the Electroreduction of CO_2 : A Comparison of Theoretical Approaches. *Phys. Chem. Chem. Phys.* **2015**, *17* (21), 13949–13963. https://doi.org/10.1039/C5CP00946D.
(27) Steinmann, S. N.; Sautet, P. Assessing a First-Principles Model of an Electrochemical Interface by Comparison with Experiment. *J. Phys. Chem. C* **2016**, *120* (10), 5619–5623. https://doi.org/10.1021/acs.jpcc.6b01938.
(28) Goodpaster, J. D.; Bell, A. T.; Head-Gordon, M. Identification of Possible Pathways for C–C Bond Formation during Electrochemical Reduction of CO_2 : New Theoretical Insights from an Improved Electrochemical Model. *J. Phys. Chem. Lett.* **2016**, *7* (8), 1471–1477. https://doi.org/10.1021/acs.jpclett.6b00358.
(29) Mathew, K.; Sundararaman, R.; Letchworth-Weaver, K.; Arias, T. A.; Hennig, R. G. Implicit Solvation Model for Density-Functional Study of Nanocrystal Surfaces and Reaction Pathways. *J. Chem. Phys.* **2014**, *140* (8), 084106. https://doi.org/10.1063/1.4865107.
(30) Nozières, P.; Pines, D. Correlation Energy of a Free Electron Gas. *Phys. Rev.* **1958**, *111* (2), 442–454. https://doi.org/10.1103/PhysRev.111.442.
(31) Harl, J.; Kresse, G. Cohesive Energy Curves for Noble Gas Solids Calculated by Adiabatic Connection Fluctuation-Dissipation Theory. *Phys. Rev. B* **2008**, *77* (4), 045136. https://doi.org/10.1103/PhysRevB.77.045136.

(32) Gunnarsson, O.; Lundqvist, B. I. Exchange and Correlation in Atoms, Molecules, and Solids by the Spin-Density-Functional Formalism. *Phys. Rev. B* **1976**, *13* (10), 4274–4298. https://doi.org/10.1103/PhysRevB.13.4274.
(33) Langreth, D. C.; Perdew, J. P. Exchange-Correlation Energy of a Metallic Surface: Wave-Vector Analysis. *Phys. Rev. B* **1977**, *15* (6), 2884–2901. https://doi.org/10.1103/PhysRevB.15.2884.
(34) Wei, Z.; Göltl, F.; Sautet, P. Diffusion Barriers for Carbon Monoxide on the Cu(001) Surface Using Many-Body Perturbation Theory and Various Density Functionals. *J. Chem. Theory Comput.* **2021**, *17* (12), 7862–7872. https://doi.org/10.1021/acs.jctc.1c00946.
(35) Wei, Z.; Sautet, P. Improving the Accuracy of Modelling CO_2 Electroreduction on Copper Using Many-Body Perturbation Theory. *Angew. Chem. Int. Ed.* **2022**, *61* (43), e202210060. https://doi.org/10.1002/anie.202210060.
(36) Wei, Z.; Göltl, F.; Steinmann, S. N.; Sautet, P. Modeling Electrochemical Processes with Grand Canonical Treatment of Many-Body Perturbation Theory. *J. Phys. Chem. Lett.* **2022**, *13* (26), 6079–6084. https://doi.org/10.1021/acs.jpclett.2c01376.
(37) Cheng, D.; Wei, Z.; Sautet, P. Elucidating the Proton Source for CO_2 Electro-Reduction on Cu(100) Using Many-Body Perturbation Theory. *J. Am. Chem. Soc.* **2025**, *147* (13), 10954–10965. https://doi.org/10.1021/jacs.4c14108.
(38) Jović, V. D.; Jović, B. M. EIS and Differential Capacitance Measurements onto Single Crystal Faces in Different Solutions. *J. Electroanal. Chem.* **2003**, *541*, 13–21. https://doi.org/10.1016/S0022-0728(02)01310-4.
(39) P. Schouten, K. J.; Gallent, E. P.; Koper, M. T. M. The Electrochemical Characterization of Copper Single-Crystal Electrodes in Alkaline Media. *J. Electroanal. Chem.* **2013**, *699*, 6–9. https://doi.org/10.1016/j.jelechem.2013.03.018.
(40) Gunathunge, C. M.; Li, J.; Li, X.; Hong, J. J.; Waegele, M. M. Revealing the Predominant Surface Facets of Rough Cu Electrodes under Electrochemical Conditions. *ACS Catal.* **2020**, *10* (12), 6908–6923. https://doi.org/10.1021/acscatal.9b05532.
(41) Wei, J.; Zhang, Z.; Gee, W.; Wei, Y.; Zhou, Y.-W.; Herran, M.; Sautet, P.; Alexandrova, A. N.; Roldan Cuenya, B.; Kley, C. S. Role of Surface Hydroxyls in Atomic-Scale Copper Restructuring during CO Electroreduction. *J. Am. Chem. Soc.* **2025**, *147* (49), 45178–45188. https://doi.org/10.1021/jacs.5c14516.
(42) Shao, F.; Xia, Z.; You, F.; Wong, J. K.; Low, Q. H.; Xiao, H.; Yeo, B. S. Surface Water as an Initial Proton Source for the Electrochemical CO Reduction Reaction on Copper Surfaces. *Angew. Chem. Int. Ed.* **2023**, *62* (3), e202214210. https://doi.org/10.1002/anie.202214210.
(43) Harl, J.; Kresse, G. Accurate Bulk Properties from Approximate Many-Body Techniques. *Phys. Rev. Lett.* **2009**, *103* (5), 056401. https://doi.org/10.1103/PhysRevLett.103.056401.
(44) Adler, S. L. Quantum Theory of the Dielectric Constant in Real Solids. *Phys. Rev.* **1962**, *126* (2), 413–420. https://doi.org/10.1103/PhysRev.126.413.
(45) Wiser, N. Dielectric Constant with Local Field Effects Included. *Phys. Rev.* **1963**, *129* (1), 62–69. https://doi.org/10.1103/PhysRev.129.62.
(46) Nørskov, J. K.; Rossmeisl, J.; Logadottir, A.; Lindqvist, L.; Kitchin, J. R.; Bligaard, T.; Jónsson, H. Origin of the Overpotential for Oxygen Reduction at a Fuel-Cell Cathode. *J. Phys. Chem. B* **2004**, *108* (46), 17886–17892. https://doi.org/10.1021/jp047349j.
(47) Cheng, D.; Wei, Z.; Zhang, Z.; Broekmann, P.; Alexandrova, A. N.; Sautet, P. Restructuring and Activation of Cu(111) under Electrocatalytic Reduction Conditions. *Angew. Chem.* **2023**, *135* (20), e202218575. https://doi.org/10.1002/ange.202218575.

(48) Mathew, K.; Sundararaman, R.; Letchworth-Weaver, K.; Arias, T. A.; Hennig, R. G. Implicit Solvation Model for Density-Functional Study of Nanocrystal Surfaces and Reaction Pathways. *J. Chem. Phys.* **2014**, *140* (8), 084106. https://doi.org/10.1063/1.4865107.
(49) Kresse, G.; Hafner, J. *Ab Initio* Molecular Dynamics for Liquid Metals. *Phys. Rev. B* **1993**, *47* (1), 558–561. https://doi.org/10.1103/PhysRevB.47.558.
(50) Blöchl, P. E. Projector Augmented-Wave Method. *Phys. Rev. B* **1994**, *50* (24), 17953–17979. https://doi.org/10.1103/PhysRevB.50.17953.
(51) Cheng, D.; Nguyen, K.-L. C.; Sumaria, V.; Wei, Z.; Zhang, Z.; Gee, W.; Li, Y.; Morales-Guio, C. G.; Heyde, M.; Roldan Cuenya, B.; Alexandrova, A. N.; Sautet, P. Structure Sensitivity and Catalyst Restructuring for CO2 Electro-Reduction on Copper. *Nat. Commun.* **2025**, *16* (1), 4064. https://doi.org/10.1038/s41467-025-59267-3.
(52) Gauthier, J. A.; Lin, Z.; Head-Gordon, M.; Bell, A. T. Pathways for the Formation of C_{2+} Products under Alkaline Conditions during the Electrochemical Reduction of CO_2. *ACS Energy Lett.* **2022**, *7* (5), 1679–1686. https://doi.org/10.1021/acsenergylett.2c00167.
(53) Peng, H.; Tang, M. T.; Liu, X.; Schlexer Lamoureux, P.; Bajdich, M.; Abild-Pedersen, F. The Role of Atomic Carbon in Directing Electrochemical $CO_{(2)}$ Reduction to Multicarbon Products. *Energy Environ. Sci.* **2021**, *14* (1), 473–482. https://doi.org/10.1039/D0EE02826F.
(54) Liu, P.; Wang, J.; Avargues, N.; Verdi, C.; Singraber, A.; Karsai, F.; Chen, X.-Q.; Kresse, G. Combining Machine Learning and Many-Body Calculations: Coverage-Dependent Adsorption of CO on Rh(111). *Phys. Rev. Lett.* **2023**, *130* (7), 078001. https://doi.org/10.1103/PhysRevLett.130.078001.

TOC Graphic